MATERIALS SCIENCE

High-K dielectric sulfur-selenium alloys

Sandhya Susarla[1], Thierry Tsafack[1], Peter Samora Owuor[1], Anand B. Puthirath[1], Jordan A. Hachtel[2], Ganguli Babu[1], Amey Apte[1], BenMaan I. Jawdat[1], Martin S. Hilario[3], Albert Lerma[4], Hector A. Calderon[5], Francisco C. Robles Hernandez[6], David W. Tam[7], Tong Li[8], Andrew R. Lupini[9], Juan Carlos Idrobo[2], Jun Lou[1], Bingqing Wei[8], Pengcheng Dai[7], Chandra Sekhar Tiwary[1,10]*, Pulickel M. Ajayan[1]*

Upcoming advancements in flexible technology require mechanically compliant dielectric materials. Current dielectrics have either high dielectric constant, K (e.g., metal oxides) or good flexibility (e.g., polymers). Here, we achieve a golden mean of these properties and obtain a lightweight, viscoelastic, high-K dielectric material by combining two nonpolar, brittle constituents, namely, sulfur (S) and selenium (Se). This S-Se alloy retains polymer-like mechanical flexibility along with a dielectric strength (40 kV/mm) and a high dielectric constant (K = 74 at 1 MHz) similar to those of established metal oxides. Our theoretical model suggests that the principal reason is the strong dipole moment generated due to the unique structural orientation between S and Se atoms. The S-Se alloys can bridge the chasm between mechanically soft and high-K dielectric materials toward several flexible device applications.

INTRODUCTION

Dielectric materials in the form of insulators, capacitors, and resonators are important passive components in most electrical and electronic circuits used for energy storage, pulsed power, power conditioning, band-pass filtering, sensing, and microelectronics (*1*–*6*). The current "flexible" technology wave in these areas (*5*, *7*–*10*) has increased the demand for flexible high-K dielectric materials (*11*, *12*). Conventional dielectrics are either ceramics or polymers (*3*, *8*, *12*–*15*). Ceramic dielectrics are high-K brittle materials such as $BaTiO_3$, HfO_2, SiO_2, and $SrTiO_3$ with large losses and low breakdown voltage (*3*, *13*), whereas polymers such as polyvinylidene difluoride (PVDF), polyamide, and rubber have high dielectric strength and flexibility but low-K values limit their application in devices (*8*, *12*–*15*). To get the best of both polymer and ceramic dielectrics, polymer composites with various high-K ceramic nanoparticle fillers have been considered (*16*, *17*). We eschew the composite approach in this work to develop a new monolithic, lightweight, flexible, and high-K dielectric material by combining two common nonpolar, brittle constituents, sulfur (S) and selenium (Se), through a facile scalable comelting process. S and Se are miscible in all ratios and form chalcogenide alloys whose optical and photoconduction properties have been studied in the literature (*18*, *19*). The comelted S-Se alloy exhibits viscoelastic behavior and mechanical flexibility like soft polymers. The dielectric constant ($K = 74$ at 1 MHz) and the dielectric strength (40 kV/mm) are comparable to some of the conventional metal oxides ($0 < K < 80$) and 10 times higher than polymers ($1 < K < 10$). There is a 13 times increment in the dielectric constant as compared to the individual components S and Se. Theoretical models suggest that such polarization in S-Se is the result of a strong dipole moment generated because of the unique structural and electronic interactions between S and Se. These chalcogen alloys could fill the gap for soft high-K dielectric materials in several flexible device applications.

RESULTS

Pure S and Se powders were mixed in a mortar and pestle in equimolar ratios (Materials and Methods) and comelted at 573 K in an Ar atmosphere (Fig. 1, A to C). Pure S shows the presence of three Raman peaks corresponding to 152, 218, and 471 cm^{-1} S-S phonon vibrations. On the other hand, pure Se shows the presence of two phonon modes at 145 and 234 cm^{-1}, attributing to Se-Se bond vibrations. The Raman spectrum of the S-Se alloy in Fig. 1D shows the presence of two peaks attributed to S-Se bonds (255 and 351 cm^{-1}) apart from Se-Se phonon vibrations (239 cm^{-1}). The formation of the S-Se alloy causes a small shift in Se-Se phonon modes (*20*). X-ray diffraction (XRD) results shown in Fig. 1E indicate that the S-Se alloy adopts a monoclinic structure, with the planes marked with blue ink. The additional peaks, indicated by black ink in Fig. 1E, correspond to residual hexagonal Se (DB: 04-008-1850; DB: 04-003-6030). The detailed indexing of all the XRD peaks is described in table S1. The large background signal in XRD data indicates that the comelted alloy is semicrystalline in nature. XRD of pure S and Se reveals that they adopt a monoclinic and hexagonal structure, respectively (fig. S1). Thermogravimetric analysis (TGA) shows that the alloy's thermal stability lies in between pure S and Se. S and Se degrade at 488 and 623 K, respectively, while the alloy degrades at 573 K (Fig. 1F). The layer-type morphology of the alloys was observed under a scanning electron microscope (SEM) (Fig. 1G). The absence of voids in the SEM images indicates that the material is dense and nonporous. Optical and SEM images of other concentrations and pure S and Se are discussed in figs. S2 and S4. The elemental composition of the S-Se alloys was confirmed by x-ray photoelectron spectroscopy (XPS). Figure 1H shows four peaks in S 2p region in alloys corresponding to spin states of Se $3p_{3/2}$, Se $3p_{1/2}$, S $2p_{3/2}$, and S $2p_{1/2}$. The spin-split peak of S 2p in the alloy region shifts to the lower energy due to the presence of Se, indicating the development of negative charge over S. In a similar fashion, Se 3d peaks of the alloy shift toward the higher energy side in the presence of S, indicating the development of

[1]Department of Materials Science and Nano-engineering, Rice University, Houston, TX 77005, USA. [2]Center for Nanophase Materials Sciences, Oak Ridge National Laboratory, Oak Ridge, TN 37831, USA. [3]Air Force Research Laboratory, Kirtland Air Force Base, Albuquerque, NM 87117, USA. [4]Leidos Inc., Albuquerque, NM 87106, USA. [5]Mechanical Engineering Technology, University of Houston, Houston, TX 77204, USA. [6]Instituto Politécnico Nacional, ESFM, UPALM, Zacatenco, Mexico CDMX 07338, Mexico. [7]Department of Physics and Astronomy, Rice University, Houston, TX 77005, USA. [8]Department of Mechanical Engineering, University of Delaware, Newark, DE 19716, USA. [9]Materials Science and Technology Division, Oak Ridge National Laboratory, Oak Ridge, TN 37831, USA. [10]Department of Materials Science and Engineering, Indian Institute of Technology, Kharagpur-721302, India.
*Corresponding author. Email: cst.iisc@gmail.com (C.S.T.); ajayan@rice.edu (P.M.A.)

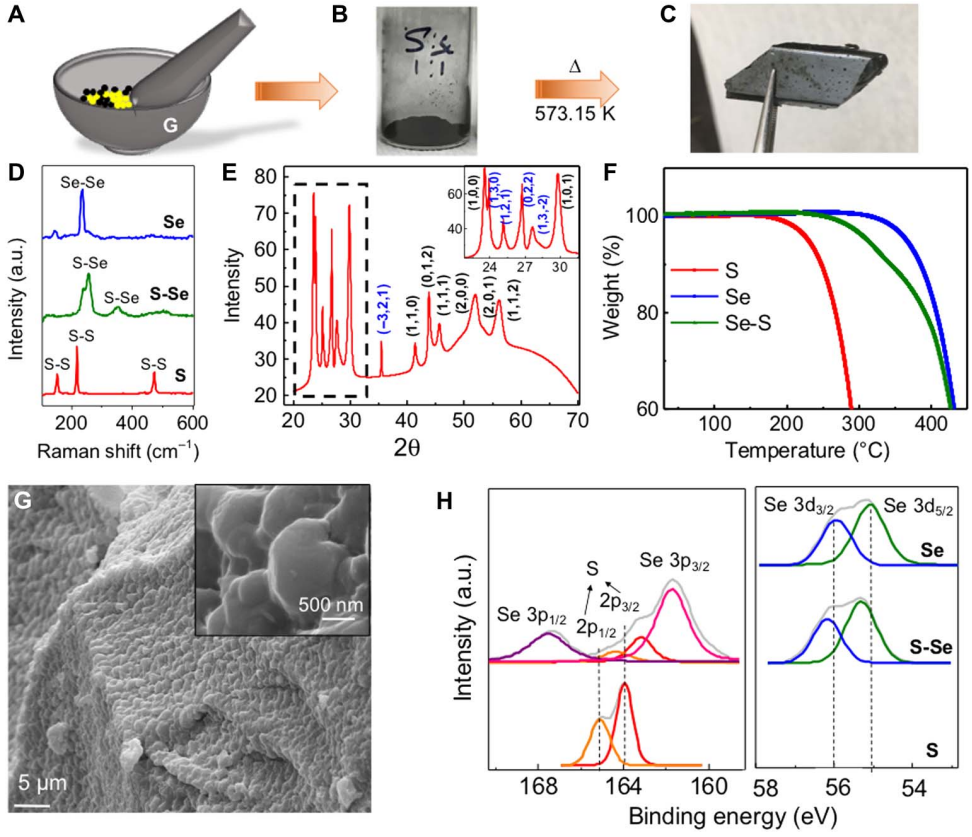

Fig. 1. Structural characterization of the S-Se alloy. (**A**) Schematic representing the procedure of synthesis of the S-Se alloy. S and Se are taken in a 1:1 molar ratio in a mortar and pestle. (**B**) Ground powder mixture of S and Se. (**C**) S-Se alloy obtained after comelting at 573 K. Photo credit for (C): Sandhya Susarla, Rice University. (**D**) Raman spectrum of the comelted pure S, S-Se alloy, and pure Se. (**E**) XRD of the comelted pure S, S-Se alloy, and pure Se. (**F**) TGA of pure S, pure Se, and S-Se alloys showing degradation at 488, 573, and 623 K, respectively. (**G**) SEM of the S-Se alloy showing a layered structure and the absence of voids. The inset of the high-magnification image details the size of each flake. (**H**) Elemental analysis of XPS spectrum of the comelted pure S, S-Se alloy, and pure Se, showing the amount of shift in the individual spin-split peak of S and Se with alloying.

positive charge over Se (*21*). Details about the calculation of composition of alloys from XPS are mentioned in table S2. The composition of the alloy is further characterized through electron energy-loss spectroscopy (EELS), which exhibits both the Se M-edge at 57 eV and the S L-edge at 165 eV, shown in fig. S6. The structural information of the S-Se alloy was also determined at the micro- and nanoscale using selected-area electron diffraction, nanodiffraction, and high-resolution transmission electron microscopy (HRTEM) (details are discussed in figs. S7 to S10).

The molecular arrangement of S-Se was further probed by ab initio calculation. Unlike S that has been extensively studied and shown to exist in a variety of allotropes, S_n, with $n > 30$, the allotropy of Se has so far shown only a few selected ones in the solid phase, Se_m, with m being 8 or 6 (making Se_m an eight- or six-member ring), or a large number, making Se_m effectively an arrangement of infinite Se chains (*22*). However, at the synthesis temperature of 573 K, octaselenium (Se_8) and octasulfur (S_8) appear to be the most abundant and the most stable of their respective allotropes (*22*, *23*). They both adopt a crown conformation with D4h point group symmetry, with Se-Se bond length being roughly 1.14 times the S-S bond length. To derive the geometry of the Se-S monomer that constitutes the building block of the polymeric structure, we analyzed adjacent (Fig. 2A), layered (Fig. 2B), and transverse (Fig. 2C) orientations in terms of formation energy (ΔH), HOMO-LUMO energy ($\Delta E_{\text{HOMO-LUMO}}$), net dipole moment ($\mu$), equilibrium constant (K), infrared (ν_{IR}), and Raman (ν_{Raman}) frequencies corresponding to the highest peaks. Discussion on each parameter is shown in table S3. The transverse orientation of S_8 and Se_8 (Fig. 2C) displays the highest polarity (μ = 2.8135 D) as well as very high IR (374.105 cm^{-1}) and Raman (374.105 cm^{-1}) frequencies at the highest peaks. This signals the presence of both strong and weak bonds between the two molecules. The addition of the good attraction ($\Delta H = -1.031$ eV) to the high stability ($\Delta E_{\text{HOMO-LUMO}} = 3.124$ eV) of the orientation makes it the likeliest orientation in the polymer unit. The orbital mixing diagram in Fig. 2E shows good HOMO-1, HOMO, LUMO, and LUMO+1 Se_8S_8 orbitals resulting from the overlap between Se_8 and S_8 HOMO/LUMO and LUMO/HOMO orbital interactions. Figure 2 (F and G) shows the entire IR and Raman spectra of Se_8S_8. The close matching of theoretical Raman peaks with the experimental data (Fig. 1D) confirms the existence of transverse orientation of S and Se in alloy. In the insets, the displacement vectors (blue arrows) at the four S atoms closer to Se_8 indicate that those atoms contribute chiefly to the vibrational bending modes of the entire structure, with the closest S atom to Se_8 being the major contributor. The orange arrow going through Se_8 from the S atom with the longest displacement vector is an Se_8S_8 dipole moment, indicating a strong polarization (see fig. S11 for further evidence) from S_8 (mostly negatively charged) to Se_8 (mostly positively charged), in agreement with the XPS results (Fig. 1H). The existence of Se-Se phonon vibrations in experimental Raman spectra (Fig. 1D) indicates that a

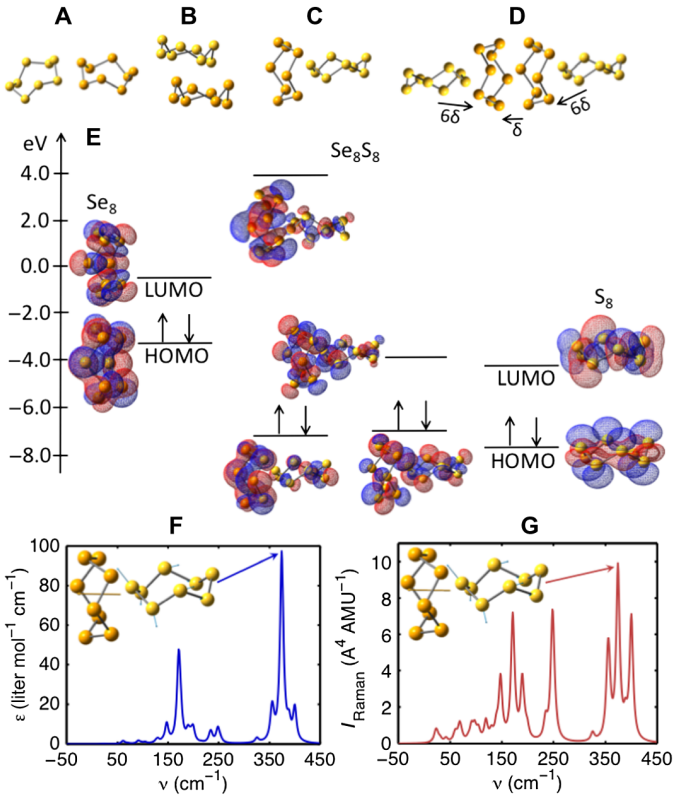

Fig. 2. Ab initio calculations done on S-Se alloys. Examples of adjacent (**A**), layered (**B**), and transverse (**C**) orientations for S_8S_8, Se_8Se_8, and Se_8Se. (**D**) Plausible polymer unit for the material. (**E**) HOMO-LUMO/LUMO-HOMO orbital mixing diagram between Se_8 and S_8, Se_8S_8 HOMO-1, HOMO, LUMO, and LUMO+1 orbitals shown in the middle. Calculated IR spectrum (**F**) and Raman spectrum (**G**) for Se_8S_8. The inset shows the displacement vectors (blue arrow on the four closest S atoms to Se_8) and dipole moment (orange arrow).

combination of two identical transverse orientations between Se_8 and S_8, as depicted in Fig. 2D displaying a layered orientation between Se_8 and Se_8, constitutes a basic polymeric structure for the material. The small dipole moment (δ) between Se_8 and Se_8 is likely to respond repulsively to a compression of the S_8Se_8 structure from the left and the Se_8S_8 structure from the right. Both are kept immobile by opposite forces coming from bigger dipoles.

The possibility of resistance to compression due to transverse arrangement was experimentally verified by conducting compression tests on pure S, pure Se, and S-Se alloys. Snapshots from the compression tests conducted on pure S and Se show that they fracture easily upon application of load and display brittle behavior (Fig. 3, A and C). On the other hand, when the load is applied on the S-Se alloy, instead of fracturing, it undergoes high-strain deformation to a thin sheet and recovers its original shape upon removal of load (Fig. 3B). It is interesting to note that this behavior is only observed in the near equimolar ratios of S and Se (fig. S12). From the load-displacement curve as shown in Fig. 3D, it is observed that, while pure S and Se blocks fail at 0.2 kN, S-Se alloys of similar dimensions sustain loads up to 25 kN without fracturing. The corresponding stress-strain curves show that the alloys sustain stresses as high as 0.4 GPa (fig. S13A). The load-displacement and stress-strain curves resemble those of elastomeric materials. To quantify the amount of mechanical recovery, we measured the height of the sample during the experiment. It is observed that the alloy recovers 40% strain immediately after the release of load and 96% strain after 10 min (Fig. 3E). Furthermore, cyclic tensile tests were done using dynamic mechanical analysis (DMA) to identify the type of elastic behavior (Fig. 3G). The hysteresis (red shaded portion) in the cyclic loading-unloading curve in the tensile test confirms the viscoelastic behavior of the alloy (*24*). Next, temperature-dependent (−20° to 60°C) DMA cyclic tensile tests were done on the S-Se material to determine its dynamic modulus, storage modulus, loss modulus, and damping effects (tanδ) (Fig. 3H). At room temperature (25°C), the storage, loss, and dynamic modulus were 150, 80, and 170 MPa, respectively. The glass transition temperature (T_g) of the alloy measured from differential scanning calorimetry is 10° ± 1°C (fig. S13B). The T_g measured here is in agreement with the previous report on S-Se systems (*25*) and suggests that the synthesized semicrystalline material behaves elastically at room temperature (above the glass transition temperature of the amorphous phase in the material). The stiffness of the alloy as determined by DMA increases at low loading cycles but decreases as the cycle number increases (fig. S13C). The local elastic modulus of the alloy was mapped by atomic force microscopy (AFM) and shows that it has an average stiffness of 3 GPa (Fig. 3F).

As seen earlier from ab initio calculations, a significant chemical affinity exists between S_8 and Se_8 in the perpendicular orientation. Both molecules are individually nonpolar, but when brought together perpendicularly, a charge delocalization from the most electronegative elements (S) to the others (Se) generates a significant dipole moment between the two molecules (+2.81 D) (Fig. 4A). The existence of a dipole moment in S-Se was experimentally verified by measuring the complex impedance in the Autolab 302 electrochemical workstation using the module FRA32M. The dielectric constant of the S-Se alloy was estimated by calculating the capacitance of the material obtained in the impedance measurement. For this purpose, 10 nm of Au was coated on the top and bottom surfaces and the impedance measurement was carried out. More details on the calculation of the dielectric constant are discussed in Materials and Methods. Figure 4B shows the variation of complex impendence (Z^*) and phase (Θ) as functions of the frequency at a bias of 0 V and a signal amplitude of 10 mV. The presence of a perfect semicircle in the Nyquist plots (Fig. 4C) confirms the capacitive behavior in the alloys. To determine the capacitance of S-Se to calculate the dielectric constant, we fitted the Nyquist curves to ideal parallel resistor and capacitor equivalent circuit. Details about the calculation of the dielectric constant are described in Supplementary Materials and Methods. The calculated dielectric constant and loss factor as a function of frequency are shown in Fig. 4 (D and E). The large dielectric constant (K) and high loss factor at low frequencies (1 Hz to 1 kHz) are attributed to Maxwell-Wagner-Sillars interfacial polarization effects. Hence, the measurement in this range has not been taken as a genuine dielectric constant value (Fig. 4D) (*26*). K immediately drops to 74 at 1-kHz frequencies and stays at 74 from kilohertz to megahertz frequencies. The large and stable value of the dielectric constant from 1 kHz to 1 MHz indicates the presence of strong dipolar interactions as predicted by ab initio calculations (Fig. 4, A and D, inset). The impedance measurement of the alloy was repeated with alloys of different thicknesses to ensure the consistency in the measurement of the dielectric constant value. The dielectric constant at kilohertz to megahertz frequencies is similar for samples with different thicknesses (fig. S14A and table S4). At higher frequencies (100 GHz), the response time of the dipoles to the electromagnetic field becomes much less than the oscillation of the field and the dielectric constant drops to 4.5 (fig. S14B). The material's inherent dissipation of electromagnetic energy, i.e., dielectric loss, is determined

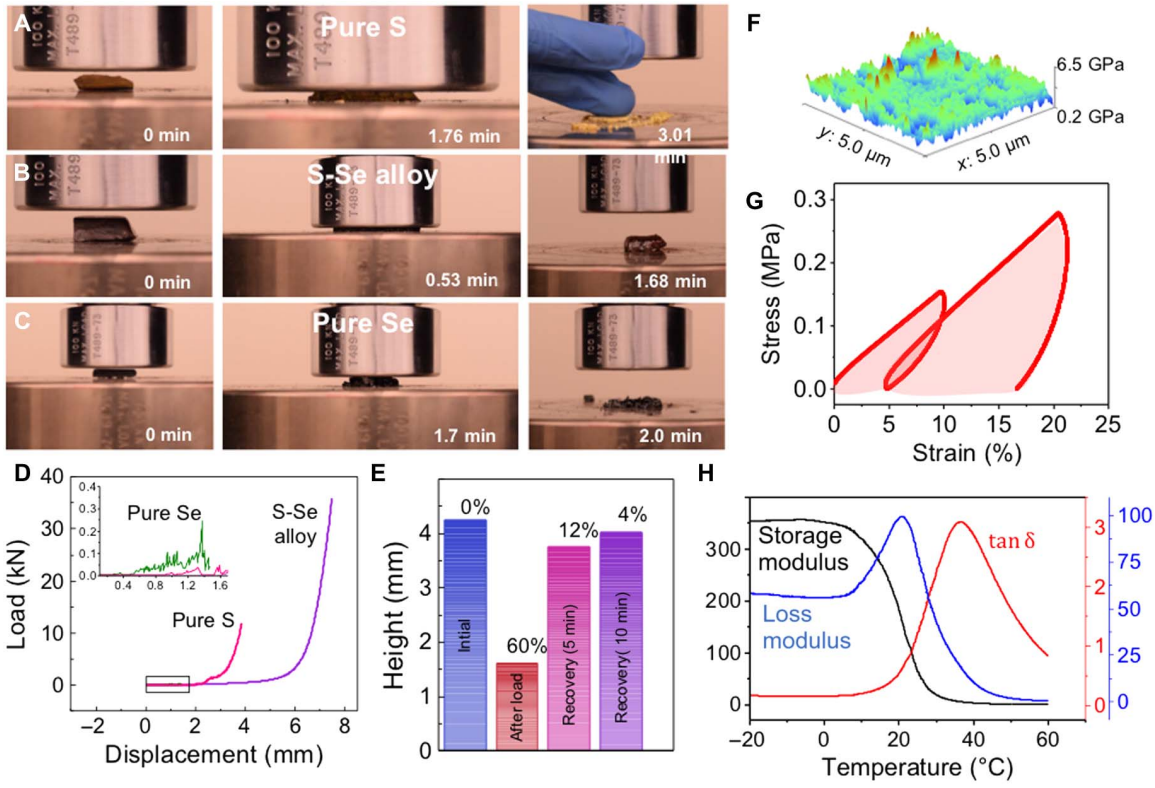

Fig. 3. Mechanical properties of S-Se alloys. Snapshots taken at different time intervals of compression test done. (**A**) Pure S. (**B**) S-Se alloy. (**C**) Pure Se. The S-Se alloy shows excellent recoverability. Photo credit for (A) to (C): Mohammad Sajadi and Peter Owuor, Rice University. (**D**) Load-displacement curves for the compression test done on the three samples. (**E**) Height of the sample measured at different time intervals during recovery. The strain values at those instances are also indicated above the bar column. (**F**) AFM modulus mapping of S-Se alloys taken over 5 μm × 5 μm area. (**G**) Cyclic tensile tests carried out in DMA, giving rise to hysteresis (red shaded area) in the load-unload curves, thus confirming the viscoelastic behavior. (**H**) Variation of storage modulus, loss modulus, and damping (tanδ) with temperature.

by the imaginary part of the dielectric constant. The dielectric loss was calculated by the phase difference in the impedance at various frequencies (Fig. 4B). The remarkable dielectric stability of the S-Se alloys at kilohertz to megahertz frequencies is evidenced by the low values of loss tangent (0.001), unlike other conventional ceramics such as HfO_2 and TiO_2 (Fig. 4E) (*3*, *13*). At higher frequencies (100 Hz), the dielectric loss (0.8) is significant as compared to other polymer materials in this frequency range, which may lead to applicability as an absorber at higher frequencies (for example, in the damping of unwanted higher-order resonances in devices) (fig. S14C) (*27*). At higher bias (1 V), the capacitance of the alloy is reduced. This occurs because of the change in the shape of the alloy upon application of electrical potential, a common phenomenon for dielectric elastomers (fig. S14D). It is interesting to note that pure S and Se are nonpolar with dielectric constants of 3 and 6, respectively (fig. S14, E and F). There is a 13 times increase in the dielectric constant when S and Se are combined. It is evident that at a frequency of 1 MHz, among common polymer dielectric materials such as Polypropylene (PP), Polystyrene (PS), and PolyVinylidene Fluoride (PVDF) ($0 < K < 10$), the S-Se alloy has comparable flexibility and an eightfold increase in the dielectric constant. On the other hand, among the common metal oxides used in the capacitor and semiconductor industries such as HfO_2, Ta_2O_5, Al_2O_3, and SiO_2, this material has a comparable dielectric constant ($0 < K < 80$) with added flexibility. Thus, the obtained S-Se alloys have polymer-like flexibility and a dielectric constant comparable to that of ceramic metal oxides. The dielectric strength of the S-Se alloy was determined by inserting the samples between two electrodes that had an approximate radius of 4 mm and an electrode gap spacing of 1 mm, with a high-voltage power supply (HVPS) connected to the electrodes. The measured dielectric strength of the alloy (40 kV/mm) is comparable to that of the common polymer dielectric materials such as PP, PS, and PVDF ($0 <$ dielectric strength < 60 kV/mm) (fig. S15) (*28*).

DISCUSSION

In summary, it is observed that surprisingly when two brittle and nonpolar chalcogen elements, S and Se, are comelted, a semicrystalline material is formed, with amorphous S-Se, monoclinic S-Se, and hexagonal Se phases. The local interaction of Se_8 and S_8 rings in the structure results in high polarization between S_8 and Se_8 and high resistance to mechanical compression due to repulsion of dipole moments between Se_8 and Se_8. This molecular-level repulsion in Se-Se bonds in S-Se alloys results in unique mechanical behavior including viscoelasticity with excellent mechanical recovery (96%), high Young's modulus among polymers (3 GPa), and T_g (9.83 ± 1.14)°C, which is below the room temperature. The polar nature of the alloy results in a high dielectric constant ($K = 74$) at 1-MHz frequency with an extremely low dielectric loss (0.001). The dielectric strength of this alloy, 40 kV/mm, is quite high among polymer materials. This cheap, scalable, lightweight, elastic, high-K dielectric could become a valuable new dielectric material, with dielectric constant comparable to that of the high-K brittle ceramic metal oxides used in the industry and flexibility comparable to that of

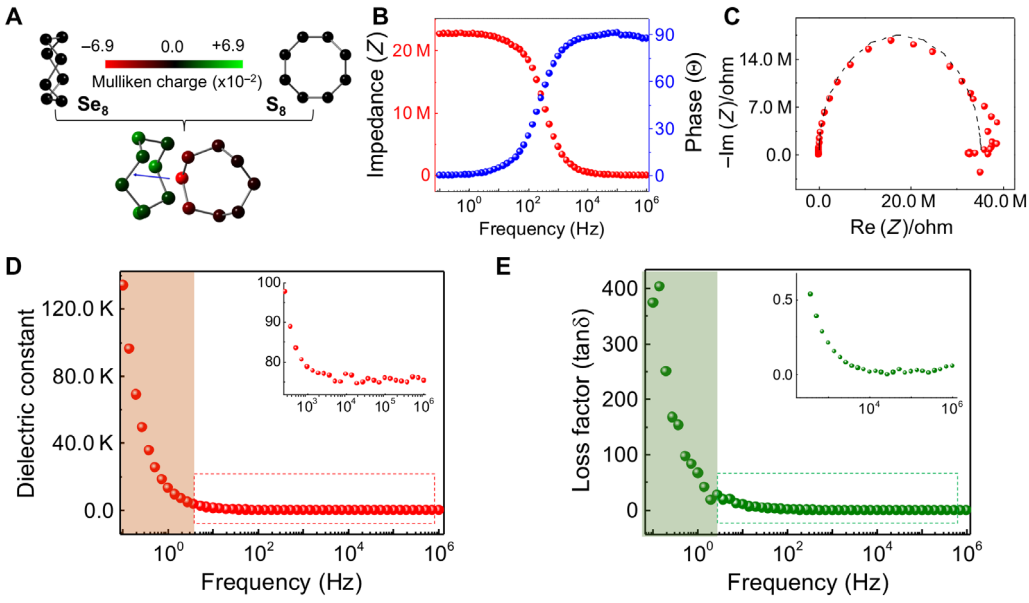

Fig. 4. Dielectric properties of S-Se alloys. (**A**) Se_8 and S_8 are initially nonpolar, zero Mulliken charge on each atom and zero net dipole moment on each molecule. However, the transverse orientation of the combination between the two molecules is a polar compound, with the highest dipole moment of all cases considered (+2.8135 D). The redder the atom, the more negative the Mulliken charge ($\times 10^{-2}$); the greener the atom, the more positive the Mulliken charge ($\times 10^{-2}$). Thus, the dipole moment goes from S_8 to Se_8 (see blue arrow). (**B**) Impedance (Z^*) and phase versus frequency plots of S-Se alloys. (**C**) Nyquist plots showing the capacitive behavior of S-Se alloys. (**D**) Variation of dielectric constant calculated from the impedance plots in (C) with frequency. The high dielectric constant in the highlighted orange region is due to electrode polarization. The stable dielectric constant, $K = 74$, in the kilohertz to megahertz frequencies is shown in the inset. (**E**) The dielectric loss factor (tanδ) as a function of frequency indicates dielectric loss at kilohertz to megahertz frequencies. The high dielectric losses at lower frequencies (highlighted green region) are due to electrode polarization.

the low-K polymer dielectrics that are considered for emerging flexible technologies.

MATERIALS AND METHODS

Sample preparation

Commercial S (99.99%; Sigma-Aldrich) and Se (99.99%; Sigma-Aldrich) were taken in equimolar ratios and mixed together in a mortar and pestle. The obtained powder was placed in an alumina boat and comelted in the furnace at a temperature of 573 K for 30 min in an Ar atmosphere. After the sample was cooled, it was taken out of the alumina mold. Another concentration of the alloys (1:1 by weight) was also prepared in the same way except for change in the initial ratio of S and Se.

Sample preparation for mechanical properties

The as-synthesized product was cut into cubes (8.67 mm × 8.67 mm × 4.25 mm) with a sharp blade. The samples were also polished slightly to ensure a flat surface for mechanical testing.

Sample preparation for in situ pressure testing

The sample for pressure was formed by casting the melt of S and Se at 513.15 K in a 1-mm-diameter stainless steel mold and was taken out of the mold by a punch.

Electrochemical properties of S/Se electrode

Li-S/Se batteries were constructed using standard 2032 coin cells, with S/Se films pressed on carbon paper. The cells were fabricated using the above electrode as the working electrode and lithium metal as the counter and reference electrode. The electrolyte that consisted of 1 M LiTFSI and lithium nitrate (0.5 M, $LiNO_3$) in tetraethylene glycol dimethyl ether (TEGDME) solvent and Celgard as a separator was used. Charge-discharge currents and specific capacities were calculated on the basis of the theoretical capacity composite electrode.

Sample preparation for impedance spectroscopy

Samples (4.00 mm × 4.900 mm × 0.374 mm) were used for measuring dielectric properties using impedance spectroscopy. As-cast samples were recasted as thin films on the Al foil, and samples of the given dimensions were cut with a blade out of the cast. Au (10 nm) was sputtered on both sides of the samples. The Au-coated samples were placed in stainless steel load cell, and impedance was measured at 0-V bias in a frequency range of 1 Hz to 1 MHz. For higher-frequency measurements (100 GHz) and dielectric strength measurements, samples (2 mm × 0.6 mm) were prepared by melting them in the corresponding Al mold.

Sample preparation for electron microscopy

Samples for TEM/scanning TEM (STEM) analysis were prepared by dispersing 1 mg of the S-Se alloy in 20 ml of ethanol solution and ultrasonicating it for 10 min.

Electron diffraction indexing

The selected area diffraction (SAD) patterns were calibrated using a gold standard. The d-spacings of the calibrated diffraction patterns were obtained using the Braggs law. The d-spacing of the polycrystalline rings is indicated in table S1. Calibrated nanodiffraction data were also indexed in the same way as the SAD pattern.

Characterization

All the Raman spectroscopy measurements were carried out with a Renishaw inVia microscope using a 532-nm laser at a power of 60.4 μW. The data were analyzed using Wire 3.3 software. XRD measurements were done using Rigaku D/Max Ultima II with Cu Kα radiation. The XRD data were analyzed using an integrated powder XRD analysis

software (PDXL2). XRD of pure S and pure Se was done for the sake of comparison. Pure S exhibited an orthorhombic structure, whereas Se exhibited a hexagonal structure. The XPS measurement was carried out with PHI Quantera XPS using Al Kα radiation operated at 200 eV. The data analysis was done using MultiPak software. The composition of the alloys was determined by calculating the area under the peak for individual spin-split S 2p and Se 3d pairs. The overlapping $Se3p_{3/2}$ region in the S 2p was not considered while calculating the composition of S in the alloys. The SAD pattern in the TEM was acquired using JEOL 2100F at 200 kV at a camera length of 20 cm. The calibration of the diffraction was done using an Au diffraction standard. Nanodiffraction and core-loss EELS were performed using a Nion aberration-corrected UltraSTEM 100 microscope, operated at an accelerating voltage of 60 kV. The nanodiffraction was performed with a convergence semiangle of 5 mrad to separate the bright-field discs in the condensed beam electron diffraction (CBED) pattern. Additional defocus was used to reduce the dose per probe position, resulting in a spatial resolution of approximately 15 nm. The nanodiffraction was acquired with a 128 × 128 position scanning grid over a field of view of 512 nm, with a dwell time of 20 ms per pixel and a beam current of 20 pA. The diffraction patterns were collected using a Hamamatsu ORCA high-speed complementary metal-oxide semiconductor (CMOS) camera with a 2048 × 2048 pixel image, which was cropped to the center of 1024 × 1024 pixels and binned to 256 × 256 pixels to achieve high signal-to-noise diffraction patterns during the fast scan. The core-loss EELS was acquired with a Gatan Enfina EEL spectrometer. The experiments were performed with a convergence semiangle of 30 mrad and an EELS collection semiangle of 48 mrad. The annular dark field (ADF) images were all acquired on the high-angle annular dark-field detector, with collection semiangles ranging from 86 to 200 mrad. The monochromated EELS experiments were performed on a Nion aberration-corrected high-energy resolution monochromated EELS-STEM (HERMESTM) at Oak Ridge National Laboratory (ORNL), operated at an accelerating voltage of 60 kV. For the band-gap measurements shown in the Supplementary Materials, a dispersion setting of 3 meV per channel was used, and the monochromator slit was set such that the zero-loss peak had a full-width at half maximum of 40 meV to find the right balance between signal and spectral resolution. The HERMES at Oak Ridge is equipped with a prototype Nion spectrometer with a Hamamatsu ORCA high-speed CMOS detector. We acquired 100 monochromated spectra with a 100-ms dwell time to leave the zero loss peak (ZLP) unsaturated and to allow an accurate energy calibration of the band gap. The beam sensitivity of the specimen caused the band gap to change during the acquisition. Hence, for the band-gap measurement reported here, only the first five frames of the 100 spectra acquisition were used to maximize the signal-to-noise ratio before significant damage occurred at the sample. The atomic-resolution TEM imaging was carried out in a TEAM 0.5 microscope with aberration-correction at 80 kV. The experimental images were taken with a spherical aberration coefficient of −0.015 mm with a focus spread of ~10 Å and in conditions of low dose. The dose rate was reduced to around 20 $e^-/Å^2s$ for images in a focal series. A focal series was used to reconstruct the exit wave and determine both phase and amplitude images with the MacTempas software. A phase image contains accurate information regarding both nature and spacings of the atomic columns in the sample volume. A focal series consisted of 40 images taken with an exposure time of 1 s and at different focus settings; between each image, there is a waiting time of approximately 1 s. Thus, the total dose in a focal series reaches approximately 800 $e^-/Å^2$. Such a dose is sufficiently low to prevent any damage because of the beam sample interaction in this investigation. A normal alignment of TEAM 0.5 was done by keeping aberrations such as C1, A1, A2, B2, A3, S3, A4, D4, B4, C5, and A5 within the confidence limits of measurement and keeping C3 at the specified value. The conditions were previously tested in different materials to image the genuine atomic arrangement of the sample by preventing any damage and keeping the required resolution of the investigated material. Digital micrograph software was used to generate the fast Fourier transformations (FFTs) and their inverse transformation (IFFT), and VESTA was used to generate the crystal projections for a more detailed analysis. The thermal stability of the alloy was investigated using TGA in an inert environment (argon, flow rate of 100 ml/min) using Q600 (TA Instruments). Approximately 10 to 15 mg of each sample were weighed before testing, and the samples were subjected to a temperature ramp of 10°C/min from 30° to 650°C.

Stiffness of the alloy was done on a DMA Q800 instrument (TA Instruments, USA). The test was conducted in a compression mode at ambient conditions with a 1-Hz cycle in a controlled strain rate mode. The mapping of mechanical stiffness was performed with AFM. The experiments were carried out with MultiMode AFM (Bruker, MA). An RTESP probe (Bruker, MA) with a resonance frequency of 530 kHz was used to map an area of 5 μm × 5 μm. The indentation depth was defined as 200 nm, and the scanning rate was 0.5 Hz. A Hertz contact model, provided in the NanoScope Analysis software (V140r1, Bruker, MA), was used to calculate the Young's modulus for each scanning point (512 × 512). Gwyddion software (*29*) was used to plot the three-dimensional profile of mechanical stiffness. The dielectric constant measurements were carried out with an Autolab 302 electrochemical workstation using a FRA32M module under 0-V bias and 10-mV signal amplitude. The ideal *RC* parallel equivalent circuit model was used to estimate the capacitance of the alloy. The circuit diagram used for calculations is shown in fig. S19. In a typical *RC* circuit model, the characteristic relaxation time or time constant, 2, of each parallel *RC* element τ is given by the product of *R* and *C*

$$\tau = RC \tag{1}$$

and

$$\omega_{max} RC = 1 \tag{2}$$

Impedance data were presented in the form of imaginary Z'' (capacitive) against real Z' (resistive). Each parallel *RC* element gave rise to a semicircle (ideally) from which the component *R* and *C* values may be extracted. *R* values were obtained from the intercepts on the Z' axis, and *C* values were obtained by applying the equation above to the frequency at the maximum of each semicircle. Because of the obtained values for these *R* and *C* components, for a parallel plate capacitor with area *A*, separation *l* between the plates, and a medium of permittivity ε′ between the plates, the capacitance is given by

$$C = \frac{\varepsilon_0 \varepsilon_r A}{d} \tag{3}$$

where *A* is the area of electrodes, *d* is the separation between the electrodes, ε_0 is the permittivity of free space (8.85×10^{-12} F/m), and ε_r is the dielectric constant of the material.

Thus, the dielectric constant values were deduced (*30*).

In situ pressure setup

For the application of uniaxial pressure, we used an instrument with a linear thruster and load cell in a feedback loop (*31*). The linear thruster was operated using compressed air, with a voltage-controlled regulator and a bleed valve controlling the inlet pressure. Mechanical force was transferred to the sample by means of concentric stainless steel tubes, with the outer tube holding an aluminum frame that supports the sample and the inner tube applying compressive force onto the sample relative. The load cell is in series with the inner tube, and the feedback loop is closed in the LabVIEW software. We mounted the apparatus horizontally with the sample positioned in the Raman laser. Pressure on the sample was estimated by measuring the transverse size of the sample. In the uniaxial pressure instrument, the S-Se sample continuously deformed over the course of several minutes at pressures as low as 1 MPa. The Raman scans were taken during the compression phase, and the sample completely expanded back to its original shape before the next pressure was applied.

Dielectric constant measurement at higher frequencies

In the dielectric measurement setup, an Agilent PNA 5222A vector network analyzer provided a low-power beam, which was boosted into the W-band (75-110 GHz) by a pair of frequency extenders. This beam was focused onto a small 0.67-inch spot by a pair of Gaussian lenses. To calculate the dielectric properties, the S parameters were first obtained by measuring the reflection and transmission coefficients. Once the S parameters were known as a function of frequency, fits were made to the data to obtain the real and imaginary parts of the dielectric constant.

Dielectric breakdown setup

The S-Se samples were tested in a high-density polyethylene dielectric holder with electrodes that had an approximate radius of 4 mm and an electrode gap spacing of the sample thickness, which was about 1 mm. One electrode was spring-loaded for retention of the sample, and the other electrode was stationary. The negative output of the HVPS was connected to the stationary electrode, while the grounded return of the HVPS was connected to the spring-loaded electrode. A Northstar (VD-120) high-voltage probe (10,000:1) was also connected to the stationary electrode to observe the breakdown voltage on a LeCroy oscilloscope. The sample was placed between the electrodes and submersed in Diala AX for testing. The ramp rate was 3 kV/s.

Electrochemical properties

Electrochemical properties such as cyclic voltammograms and charge-discharge studies were measured in the potential range from 1.7 to 2.8 V using an Autolab electrochemical workstation and an ARBIN cycle life tester, respectively.

Computational details

The structures for S_8-S_8, S_8-Se_8, Se_8-Se_8, and S_8-S_4Se_4 in adjacent (Fig. 2A), layered (Fig. 2B), and transverse (Fig. 2C) configurations were constructed in the advanced semantic chemical editor and visualization platform, Avogadro 1.2.0 (*32*). The structures were then optimized using the all-electron density functional theory equations implemented in the Gaussian 09 package with the B3LYP functional of generalized gradient approximation and the 6-31G basis set (*33*, *34*). The threshold convergence criteria for the root mean square (RMS) force, maximum displacement of atoms, maximum force, and RMS displacement were set to 0.0003, 0.0018, 0.00045, and 0.0012 a.u. (atomic units), respectively. Regarding the reactions in table S3, the energy difference between products and reactants (ΔH) as well as the HOMO-LUMO energy differences ($\Delta E_{\text{HOMO-LUMO}}$) and molecule net dipole moments (μ) were calculated. The equilibrium constant, $K = e^{-\Delta H/RT}$ (where R is the ideal gas constant, ~0.802 eV/K), was also calculated at the synthesis temperature of 513.15 K. IR and Raman spectra at different frequencies were calculated during the optimization process, and the frequencies corresponding to the highest peaks are shown in table S3.

SUPPLEMENTARY MATERIALS

Supplementary material for this article is available at http://advances.sciencemag.org/cgi/content/full/5/5/eaau9785/DC1

Supplementary Text
Fig. S1. XRD of pure S and Se.
Fig. S2. Influence of concentration in S-Se alloy synthesis.
Fig. S3. SEM micrographs of S-Se alloys synthesized at different temperatures and concentrations.
Fig. S4. Detailed SEM analysis of equimolar concentration of S-Se alloys.
Fig. S5. TGA of S-Se powder.
Fig. S6. EELS on S-Se alloy.
Fig. S7. Polycrystalline diffraction on S-Se alloy.
Fig. S8. Deconvolved diffraction patterns and the corresponding maps of different grains obtained via nanodiffraction imaging for four, five, and six output components.
Fig. S9. Nanodiffraction grain mapping of S-Se alloy.
Fig. S10. HRTEM analysis for the S-Se material with its respective FFT and d-spacing.
Fig. S11. Chemical nature of the polarity between Se_8 and S_8 in the transverse orientation.
Fig. S12. Structural characterization and mechanical properties of equal weight concentration of S-Se alloys.
Fig. S13. Mechanical behavior of S-Se alloy.
Fig. S14. Dielectric properties of equimolar S-Se alloys.
Fig. S15. Dielectric breakdown of equimolar S-Se alloy.
Fig. S16. Optical properties of equimolar S-Se alloys.
Fig. S17. In situ pressure-dependent Raman tests performed on equimolar S-Se alloys.
Fig. S18. Electrochemical properties of equimolar concentrations of S-Se alloys.
Fig. S19. Equivalent circuit used in impedance measurements and in estimating the dielectric constant of S-Se alloy.
Table S1. d-spacings of the various polycrystalline rings indicated in the SAD pattern of S-Se alloys.
Table S2. Composition of S and Se as determined by XPS spectra.
Table S3. ΔH, HOMO-LUMO gap ($\Delta E_{\text{HOMO-LUMO}}$), equilibrium constant ($K = e^{-\Delta H/RT}$ with $T = 673.15$ K), and frequencies for highest IR and Raman peaks for reactions in the first column in their adjacent, layered, and transverse orientations.
Table S4. Dielectric constant at different thicknesses of S-Se alloy.
Movie S1. Mechanical video showing the compression of S-Se alloys taken in equimolar ratio.
Movie S2. Mechanical video showing the compression of S-Se alloy taken in equal weight.
Movie S3. Mechanical video showing the compression of pure S.
Movie S4. Mechanical video showing the compression of pure S.
Reference (*35*)

REFERENCES AND NOTES

1. G. Bersuker, P. Zeitzoff, G. Brown, H. R. Huff, Dielectrics for future transistors. *Mater. Today* **7**, 26–33 (2004).
2. A. I. Kingon, J.-P. Maria, S. K. Streiffer, Alternative dielectrics to silicon dioxide for memory and logic devices. *Nature* **406**, 1032–1038 (2000).
3. J. Millan, P. Godignon, X. Perpina, A. Perez-Tomas, J. Rebollo, A survey of wide bandgap power semiconductor devices. *IEEE Trans. Power Electron.* **29**, 2155–2163 (2014).
4. Y. Cao, P. C. Irwin, K. Youns, The future of nanodielectrics in the electrical power industry. *IEEE Trans. Dielectr. Electr. Insul.* **11**, 797–807 (2004).
5. J. A. Rogers, T. Someya, Y. Huang, Materials and mechanics for stretchable electronics. *Science* **327**, 1603–1607 (2010).
6. J. A. Rogers, Y. Huang, A curvy, stretchy future for electronics. *Proc. Natl. Acad. Sci. U.S.A.* **106**, 10875–10876 (2009).
7. S. R. Forrest, The path to ubiquitous and low-cost organic electronic appliances on plastic. *Nature* **428**, 911–918 (2004).
8. J. W. Lee, H. J. Cho, J. Chun, K. N. Kim, S. Kim, C. W. Ahn, I. W. Kim, J.-Y. Kim, S.-W. Kim, C. Yang, J. M. Baik, Robust nanogenerators based on graft copolymers via control of dielectrics for remarkable output power enhancement. *Sci. Adv.* **3**, e1602902 (2017).
9. T. Sekitani, T. Someya, Human-friendly organic integrated circuits. *Mater. Today* **14**, 398–407 (2011).
10. Kenry, J. C. Yeo, C. T. Lim, Emerging flexible and wearable physical sensing platforms for healthcare and biomedical applications. *Microsyst. Nanoeng.* **2**, 16043 (2016).

11. A. E. Ostfeld, I. Deckman, A. M. Gaikwad, C. M. Lochner, A. C. Arias, Screen printed passive components for flexible power electronics. *Sci. Rep.* **5**, 15959 (2015).
12. H. Moon, H. Seong, W. C. Shin, W.-T. Park, M. Kim, S. Lee, J. H. Bong, Y.-Y. Noh, B. J. Cho, S. Yoo, S. G. Im, Synthesis of ultrathin polymer insulating layers by initiated chemical vapour deposition for low-power soft electronics. *Nat. Mater.* **14**, 628–635 (2015).
13. L. Qi, L. Petersson, T. Liu, Review of recent activities on dielectric films for capacitor applications. *J. Int. Counc. Electr. Eng.* **4**, 1–6 (2014).
14. W. Wang, J. Yang, Z. Liu, Dielectric and energy storage properties of PVDF films with large area prepared by solution tape casting process. *IEEE Trans. Dielectr. Electr. Insul.* **24**, 697–703 (2017).
15. B. Chu, X. Zhou, K. Ren, B. Neese, M. Lin, Q. Wang, F. Bauer, Q. M. Zhang, A dielectric polymer with high electric energy density and fast discharge speed. *Science* **313**, 334–336 (2006).
16. Prateek, V. K. Thakur, R. K. Gupta, Recent progress on ferroelectric polymer-based nanocomposites for high energy density capacitors: Synthesis, dielectric properties, and future aspects. *Chem. Rev.* **116**, 4260–4317 (2016).
17. S. A. Paniagua, Y. Kim, K. Henry, R. Kumar, J. W. Perry, S. R. Marder, Surface-initiated polymerization from barium titanate nanoparticles for hybrid dielectric capacitors. *ACS Appl. Mater. Interfaces* **6**, 3477–3482 (2014).
18. M. F. Kotkata, M. Fustoss-Wegner, L. Toth, G. Zentai, S. A. Nouh, Photoconduction and structural properties of amorphous selenium-sulphur semiconductors. *J. Phys. D. Appl. Phys.* **26**, 456–460 (1993).
19. A. T. Ward, Molecular structure of dilute vitreous selenium-sulfur and selenium-tellurium alloys. *J. Phys. Chem.* **74**, 4110–4115 (1970).
20. A. T. Ward, Raman spectroscopy of sulfur, sulfur-selenium, and sulfur-arsenic mixtures. *J. Phys. Chem.* **72**, 4133–4139 (1968).
21. I. Lindgren, Chemical shifts in X-ray and photo-electron spectroscopy: A historical review. *J. Electron Spectros. Relat. Phenomena* **137**, 59–71 (2004).
22. V. S. Minaev, S. P. Timoshenkov, V. V. Kalugin, Structural and phase transformations in condensed selenium. *J. Optoelectron. Adv. Mater.* **7**, 1717–1741 (2005).
23. B. Meyer, Elemental sulfur. *Chem. Rev.* **76**, 367–388 (1976).
24. P. Mason, The viscoelastic behavior of rubber in extension. *J. Appl. Polym. Sci.* **1**, 63–69 (1959).
25. A. V. Tobolsky, G. D. T. Owen, A. Eisenberg, Viscoelastic properties of S-Se-As copolymers. *J. Colloid. Sci.* **17**, 717–725 (1962).
26. S. A. Khrapak, N. P. Kryuchkov, S. O. Yurchenko, H. M. Thomas, Practical thermodynamics of Yukawa systems at strong coupling. *J. Chem. Phys.* **142**, 194903 (2015).
27. A. Elhawil, L. Zhang, J. Stiens, C. De Tandt, N. A. Gotzen, G. V. Assche, R. Vounckx, A quasi-optical free-space method for dielectric constant characterization of polymer materials in mm-wave band. *IEEE Proc. Symp. LEOS Benelux Chapter* **66**, 187–190 (2007).
28. L. Berger, Dielectric strength of insulating materials. *Carbon* **1**, 2 (2006).
29. D. Nečas, P. Klapetek, Gwyddion: An open-source software for SPM data analysis. *Open Phys.* **10**, 181–188 (2012).
30. J. T. S. Irvine, D. C. Sinclair, A. R. West, Electroceramics: Characterization by impedance spectroscopy. *Adv. Mater.* **2**, 132–138 (1990).
31. D. W. Tam, Y. Song, H. Man, S. C. Cheung, Z. Yin, X. Lu, W. Wang, B. A. Frandsen, L. Liu, Z. Gong, T. U. Ito, Y. Cai, M. N. Wilson, S. Guo, K. Koshiishi, W. Tian, B. Hitti, A. Ivanov, Y. Zhao, J. W. Lynn, G. M. Luke, T. Berlijn, T. A. Maier, Y. J. Uemura, P. Dai, Uniaxial pressure effect on the magnetic ordered moment and transition temperatures in $BaFe_{2-x}T_xAs_2$ (T = Co, Ni). *Phys. Rev. B.* **95**, 060505 (2017).
32. M. D. Hanwell, D. E. Curtis, D. C. Lonie, T. Vandermeersch, E. Zurek, G. R. Hutchison, Avogadro: An advanced semantic chemical editor, visualization, and analysis platform. *J. Cheminform.* **4**, 17 (2012).
33. A. D. Becke, Density-functional exchange-energy approximation with correct asymptotic behavior. *Phys. Rev. A Gen. Phys.* **38**, 3098–3100 (1988).
34. W. J. Hehre, R. Ditchfield, J. A. Pople, Self-consistent molecular orbital methods. XII. Further extensions of Gaussian-type basis sets for use in molecular orbital studies of organic molecules. *J. Chem. Phys.* **56**, 2257–2261 (1972).
35. L. Constantinou, R. Gani, New group contribution method for estimating properties of pure compounds. *AIChE J.* **40**, 1697–1710 (1994).

Acknowledgments: We thank S. Sajadi for help in making mechanical testing videos and H. Gullapalli for technical advice. We also thank B. Hoff for technical expertise on dielectric constant measurement and S. Heidger for advice on dielectric breakdown measurements. We also thank P. Bharadwaj for inputs on ultraviolet-visible spectroscopy measurements. **Funding:** This work was supported as part of the Computational Materials Sciences Program funded by the U.S. Department of Energy (DOE), Office of Science, Basic Energy Sciences (BES) under award number DE-SC00014607. We thank the Science & Engineering Research Board (SERB) and Indo-US Science and Technology Forum (IUSSTF) for financial support in the form of postdoctoral fellowship. Microscopy research was performed as part of a user proposal at ORNL's Center for Nanophase Materials Sciences (CNMS), which is a U.S. DOE, Office of Science User Facility at the ORNL. The research was supported by the Materials Sciences and Engineering Division Office of BES, U.S. DOE and conducted, in part, using instrumentation within ORNL's Materials Characterization Core provided by UT-Battelle LLC under contract no. DE-AC05-00OR22725 with the U.S. DOE. The in situ pressure experiments on the Raman microscope were supported by the U.S. DOE, BES (award number DE-SC0012311) and the Robert A. Welch Foundation (grant C-1839) (to P.D.). **Author contributions:** S.S. wrote the major part of the paper, synthesized the material, and carried out XRD, XPS, SAED, Raman, and impedance spectroscopy measurements. T.T. performed the molecular dynamics simulations. P.S.O. and J.L. conducted the compression, DMA, and TGA tests. A.A. helped in the sample preparation for the impedance testing. G.B. and A.B.P. did the impedance measurements and Lithium battery testing. T.L. and B.W. mapped the AFM modulus of the S-Se alloys. D.W.T. and P.D. designed the in situ pressure system for Raman measurements. B.I.J. and M.S.H. carried out the dielectric constant measurements at higher frequencies. A.L. carried out the dielectric breakdown measurement. J.A.H. carried out the nanodiffraction and EELS measurements. J.C.I. and A.R.L. advised on the nanodiffraction measurements. H.A.C. and F.C.R.H. performed HRTEM measurements on the sample. C.S.T. and P.M.A. supervised the project. All authors participated in discussions and contributed to writing the manuscript. **Competing interests:** This manuscript has been authored by UT-Battelle LLC under contract no. DE-AC05-00OR22725 with the U.S. DOE. The U.S. government retains and the publisher, by accepting the article for publication, acknowledges that the U.S. government retains a nonexclusive, paid-up, irrevocable, worldwide license to publish or reproduce the published form of this manuscript, or allow others to do so, for U.S. government purposes. The DOE will provide public access of these results for federally sponsored research in accordance with the DOE Public Access Plan (http://energy.gov/downloads/doe-public-access-plan). T.T., P.S.O., S.S., P.M.A., A.B.P., and C.S.T. are inventors on a provisional patent application related to this work filed by Rice University (no. 62/713,375, filed on 1 August 2018). **Data and materials availability:** All data needed to evaluate the conclusions in the paper are present in the paper and/or the Supplementary Materials. The S-Se alloy can be provided by authors pending scientific review and a completed material transfer agreement. Requests for the materials should be submitted to the Office of Technology Transfer, Rice University, 6100 Main Street, Houston, TX 77005-1892, USA.

Submitted 2 August 2018
Accepted 29 March 2019
Published 10 May 2019
10.1126/sciadv.aau9785

Citation: S. Susarla, T. Tsafack, P. S. Owuor, A. B. Puthirath, J. A. Hachtel, G. Babu, A. Apte, B. I. Jawdat, M. S. Hilario, A. Lerma, H. A. Calderon, F. C. Robles Hernandez, D. W. Tam, T. Li, A. R. Lupini, J. C. Idrobo, J. Lou, B. Wei, P. Dai, C. S. Tiwary, P. M. Ajayan, High-K dielectric sulfur-selenium alloys. *Sci. Adv.* **5**, eaau9785 (2019).